Design and Experiment of a Macro–Micro Planar Maglev Positioning System

Mei-Yung Chen, Tzuo-Bo Lin, Shao-Kang Hung, *Member, IEEE*, and Li-Chen Fu, *Fellow, IEEE*

Abstract—In this paper, a new planar magnetic levitation (maglev) positioning system is proposed, which is capable of executing dual-axis planar motions purely involving magnetic forces. Functionally, such a mechanism behaves like a planar XY table with micrometer precision. Specifically, in this system, a new structure with an adaptive sliding-mode control (ASMC) algorithm is described, which aims to achieve the following three goals: 1) a large moving range (millimeter level); 2) precise positioning (micrometer level); and 3) fast response. The system consists of a moving carrier platform, six permanent magnets (PMs) attached to the carrier, and six electromagnets mounted on a fixed base. After exploring the characteristics of the magnetic forces between PMs and electromagnets, the general 6-DOF dynamic model of this system is derived and analyzed. Then, because of the naturally unstable behavior inherent in maglev systems, the proposed ASMC guarantees satisfactory performance of the maglev system. Experiments have successfully demonstrated the feasibility and effectiveness of the overall system.

Index Terms—Adaptive sliding-mode controller, magnetic levitation (maglev), precision positioning.

I. INTRODUCTION

IN MACROAPPLICATIONS where a large moving range is required, a common method of positioning is to employ leadscrews or linear motors [1]. Despite their advantages of high stiffness, thrust, and speed, leadscrews suffer from lost motion, stick-slip, and wind-up. Also, leadscrews cause disturbance, friction, and backlash due to the roughness of the bearing elements. Moreover, because of friction, the linear motors also have some drawbacks, such as the ripple effect and end effect that are hard to deal with. It is noteworthy that dry friction is one of the most important factors limiting the performance of high-precision positioning devices. Overcoming these, magnetic levitation (maglev) technology has evolved to be the most suitable way to improve the performances

of traditional precision mechanisms. The benefits include the following: avoidance of mechanical contact, greater positioning resolution, operation in vacuum environment, etc. In the previous research, a double-deck mechanism was adopted in the design of a dual-axis maglev system [2], [3], where the carrier is free to move along the X- and/or the Y-directions. For simplifying the mechanism of the maglev system while also trying to reduce power consumption, a planar single-layer maglev positioning system needs to be developed.

In the literature, along the stream of maglev research works, a precision 6-DOF maglev stage with planar motion capability for photolithography in semiconductor manufacturing was presented in [4]. The key element of this stage is a linear motor capable of providing forces in both vertical suspension and lateral translation without contact. The authors there designed and implemented a linear optimal multivariable controller to deal with dynamic coupling in the carrier. The work in [5] has proposed a precision control of a linear maglev actuator with a new geometric configuration. Such configuration leads to a lightweight and compact triangular frame with three struts carrying the single magnetically levitated moving part to which a number of cylindrical magnets are affixed. The researchers also proposed a kind of planar maglev system [6], where the coils' axial directions are arranged such that a path-planning mechanism and a lead–lag control methodology can be devised to achieve successful applications in nanomanufacturing. As for the work in [7] and [8], a maglev construction that utilizes switching of 2-D electromagnet arrays with regulated currents was made to drive the carrier to move in a plane. Last but not the least, a 6-DOF magnetic levitation stage (MLS) was proposed [9], consisting of a floater that can move freely within the work volume. In the built MLS, three two-axis actuators, equivalent to six single-axis actuators, are implemented to achieve six-axis actuation and are employed to suspend and drive the moving stage.

The challenge of designing a planar maglev system is how to appropriately arrange actuators and design a stabilized controller so as to achieve the objectives of a large moving range and 2-D high-precision positioning. To attain the former goal, we first build a one-axis electromagnetic actuator (EMA) in a prototype to test and verify the feasibility. From the experimental results, it is seen that the EMA positioning system has been successfully designed and implemented [10]. Based on those experiences, a prototype of a new planar maglev positioning system designed and implemented as mentioned previously is described in detail in this paper. In the new structure, the carrier's motions (both levitation and propulsion) result from a sum of repelling forces, of which each is exerted on the magnet

M.-Y. Chen is with the Department of Mechatronic Technology, National Taiwan Normal University, Taipei 10610, Taiwan (e-mail: cmy@ntnu.edu.tw).

T.-B. Lin was with National Taiwan University, Taipei 10617, Taiwan. He is now with the Realtek Semiconductor Corporation, Hsinchu 300, Taiwan (e-mail: r90921002@ntu.edu.tw).

S.-K. Hung is with National Chiao Tung University, Hsinchu 300, Taiwan (e-mail: skhung@mail.nctu.edu.tw).

L.-C. Fu is with the Department of Electrical Engineering, National Taiwan University, Taipei 10617, Taiwan (e-mail: lichen@ntu.edu.tw).

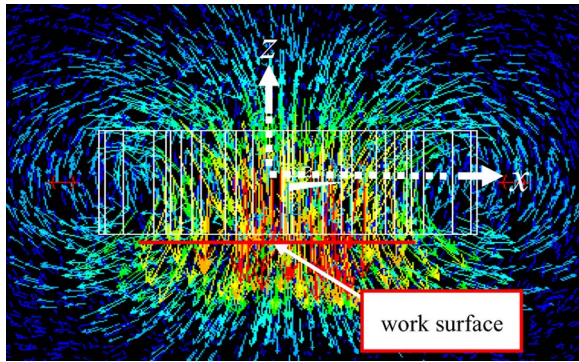Fig. 1. Magnetic flux density of a cylindrical coil.

Fig. 2. Magnetic flux density of a rectangular coil.

affixed to the carrier from its corresponding coil. Incidentally, within such structure, we provide enough gap space between the magnet and coil to let the carrier possess enough working space for creating sufficient range of motion. Note that, in this new maglev positioning system, many factors need to be taken into consideration, such as handling of system uncertainties, including parameter drift during operation caused by, for example, the following: 1) excursion of the coil temperature resulting in changes in the coil's resistance and 2) long-term operation leading to changes in the magnetization characteristics. Therefore, the desirable controller should be robust enough to deal with these uncertainties and disturbances.

In this paper, a macro–micro planar maglev positioning system, including mechanism, control, and analysis, is presented. In particular, there are five main objectives that have been addressed here: 1) to provide electromagnetic and mechanical designs for a mobile planar magnetic levitator; 2) to derive the transformation from the measured signals to the carrier's posture; 3) to establish the mathematical modeling; 4) to develop an adaptive sliding-mode control (SMC) (ASMC) to achieve 6-DOF stabilization; and 5) to perform extensive experiments to validate the proposed design and to demonstrate satisfactory performance.

The organization of this paper is as follows. In Section II, the design aspects of the implemented prototype system are described, and the model of the adopted coils is derived. In Section III, the mathematic model of the entire system dynamics is derived. In Section IV, an ASMC for the constructed maglev positioning system is proposed. Section V presents extensive experimental results which demonstrate the effectiveness of the system design and its controller. Finally, conclusions are presented in Section VI.

II. DESIGN CONCEPTS OF THE PLANAR MAGLEV SYSTEM

In this design, we need to generate a uniform magnetic field on the top surfaces of cylindrical coils so that the controller can drive the platform to move (almost) precisely in the X–Y plane. From the simulation result, a cylindrical coil (whose side view is shown in Fig. 1) can generate such a uniform magnetic field, and three of these coils can levitate the platform throughout its horizontal range. In principle, the X–Y movement of the platform is actually caused by longitudinal (toward the mouth
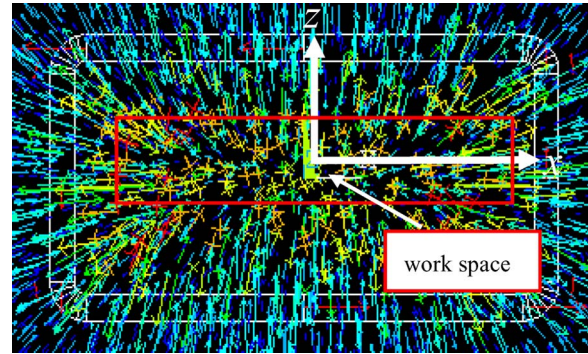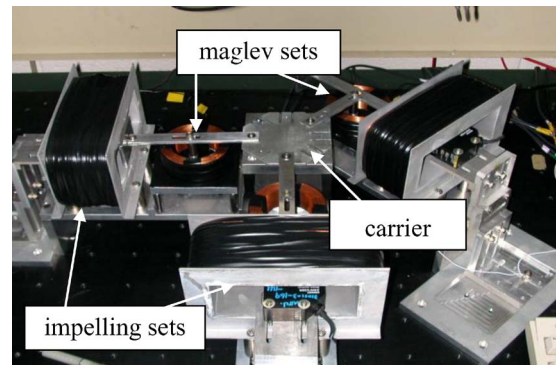

Fig. 3. Prototype of the proposed magnetically levitated system.

of the coil) as well as lateral movements of each permanent magnet (PM) inside the hollow of the associated rectangular coil. Thus, if we want to seek a large range of motion, which is an important feature in this paper, practically, the rectangular coil should have a long lateral side and a deep hollow (can result in long longitudinal travel). From the simulation result (whose front view is shown in Fig. 2), we also found that the vector field inside a rectangular coil over the lateral (cross section) plane is largely uniform, whereas it varies in a characterizable fashion over the longitudinal direction, which exactly meets our need. Apparently, the choice of rectangular coil (instead of cylindrical coil) here will be in an optimal sense since it can minimize the volume of the coil while achieving our purpose.

The planar maglev positioning system presented in this paper consists mainly of a platform, which has three hanging arms fixed on the carrier, and each hanging arm has two PMs, one at the end and the other underneath the middle of the hanging arm; three impelling sets (No.1, No.2, and No.3) which are located adjacent to the PMs located at the ends of the hanging arms and the coil of each impelling set generate the desired force for lateral motion; three maglev sets (No.4, No.5, and No.6) which are located underneath the PMs affixed to the middle of the hanging arms, and the coil of each maglev set produces the desired levitating force mainly to maintain leveling of the carrier. Figs. 3 and 4 show a physical prototype maglev system and its conceptual configuration, respectively, which we have developed. A combination of the maglev forces and the impelling forces is sufficient to control the carrier in the 6 DOF. The sizes of electromagnetics are shown in Fig. 5.
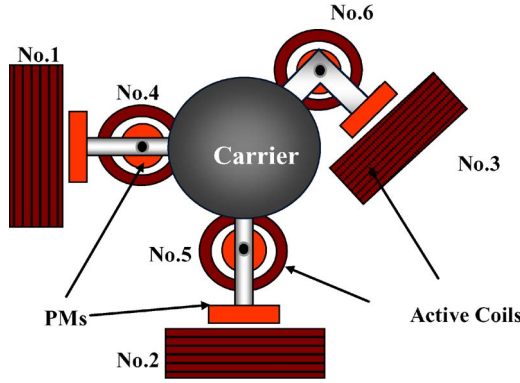
Fig. 4.   Conceptual configuration.

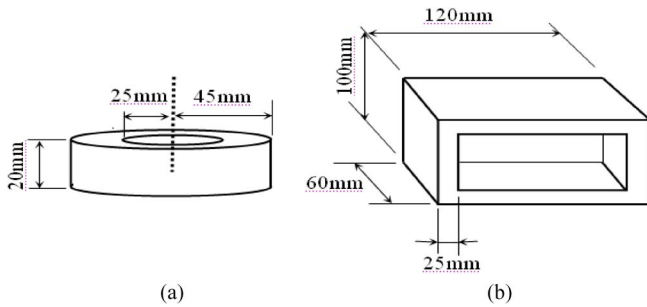(a)   (b)

Fig. 5.   Specifications of (a) cylindrical and (b) rectangular electromagnets used in this system.

To neglect the ambient electrical field, the expression for the magnetic force can be simplified as a gradient force [11], [12]

$$\vec{F} = (\vec{m} \cdot \nabla)\vec{B} \qquad (1)$$

where $\vec{m}$ is the dipole moment of the PM, $\vec{B}$ is the magnetic flux density, and $\vec{F}$ is the magnetic force between the PM and the electromagnetic coil.

We assume that the dipole moment of the PM exerted on its shape center is only in the z-direction. Thus, the force equation in (1) when applied to each electromagnetic coil can be approximately derived as follows:

Case 1)   PM in the cylindrical electromagnetic coil of the maglev set

$$F_{\mathrm{cyl},k} = \mu_0 m_{\mathrm{cyl},z} \left(\frac{\partial h_{\mathrm{cyl},k}}{\partial z} \right) \cdot I_{\mathrm{cyl}}, \quad \text{for } k = x, y, z. \quad (2)$$

Case 2)   PM in the rectangular electromagnetic coil of the impelling set

$$F_{\mathrm{rec},k} = \mu_0 m_{\mathrm{rec},z} \left(\frac{\partial h_{\mathrm{rec},k}}{\partial z} \right) \cdot I_{\mathrm{rec}}, \quad \text{for } k = x, y, z. \quad (3)$$

where h and I are the intensity of magnetic field and the current flow of a coil, respectively. For real-time controller implementation, it is not practical to establish a detailed analytical model of the magnetic force as described by (2) and (3). Thus, to solve this problem, an alternative method is to derive the empirical model based on practical measurements as a function of describing the magnetic force F in terms of the current I and position z. Here, one kind of force detector, the so-called load
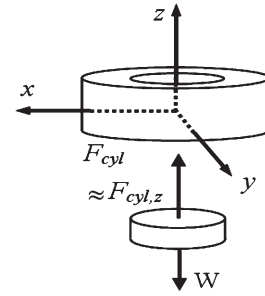

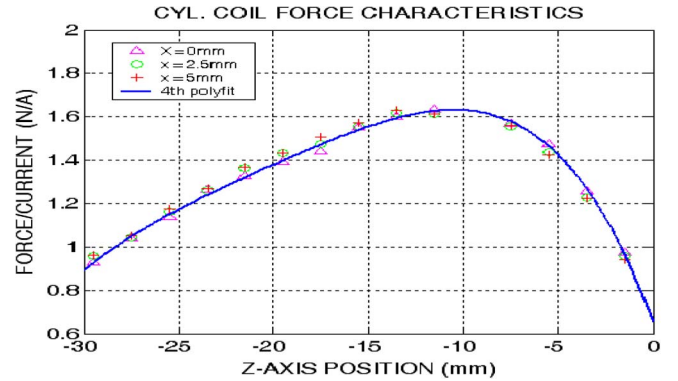Fig. 6.   Lower actuating component in the maglev set.

Fig. 7.   Magnetic force along the z-axis in the maglev sets.

cell, is used to measure the force exerted on the PM, subject to the coil's magnetic field [13]–[17].

As shown in Fig. 6, $(x, y, z)^T$ is the local coordinate of the cylindrical electromagnet in the maglev set. Several experimental results reveal that, within the desired traveling range of ± 5 mm in both the X- and Y-directions, the magnetic forces distributed on the x-axis and y-axis are much smaller than the force distributed on the z-axis. Therefore, we take care of only the force exerted on the PM along the z-axis and treat the forces distributed along other axes as disturbances. Hence, the magnetic force in the maglev set is approximated by $\vec{F}_{\mathrm{cyl}} \approx [0, 0, F_{\mathrm{cyl},z}]^T$, and based on (2), we can rewrite it as a product of a position function and the current input

$$F_{\mathrm{cyl},z} = g_{\mathrm{cyl},z}(x, y, z) I_{\mathrm{cyl}} \qquad (4)$$

where $g_{\mathrm{cyl},z} = \mu_0 m_{\mathrm{cyl}.z}(\partial h_{\mathrm{cyl}.z}/\partial z)$ and I_{cyl} represents the current input.

Due to the reason given in the previous paragraph, only the z component of the magnetic force $F_{\mathrm{cyl},z}$ in the maglev set is measured; the result is shown in Fig. 7. We set $z = 0$ at the center of the coil and let the total measuring range be $z \in [-10 \text{ mm}, -50 \text{ mm}]$ from the center through the bottom surface to the outside of the cylindrical coil. In Fig. 7, the vertical scale is the ratio of the force's magnitude to the current input (here, the current is set to 1 A), and the horizontal scale is the PM's z position with respect to the coil's center. It is worth noting, however, that the data from the force measurements made at some offset from the central axis of the electromagnet are still quite close to those measured on the central axis. The largest data discrepancy is within only 10%. Thus, it should
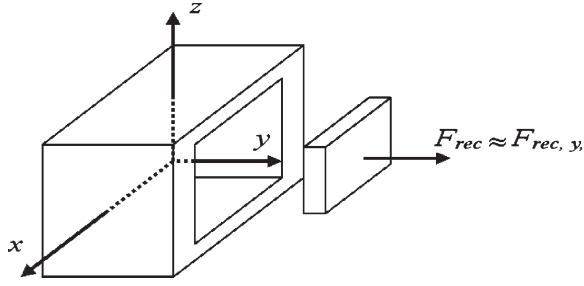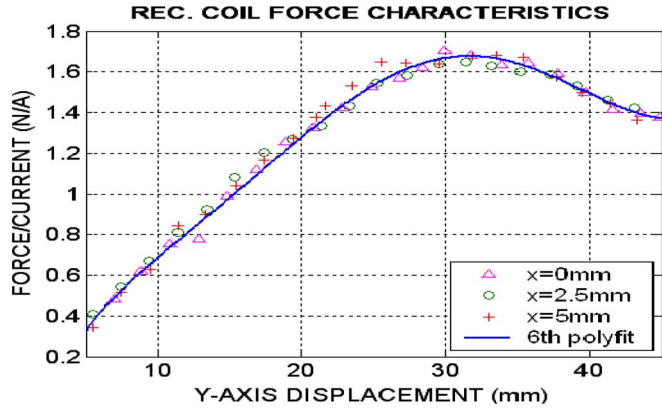
Fig. 8.   Upper actuating component in the impelling set.

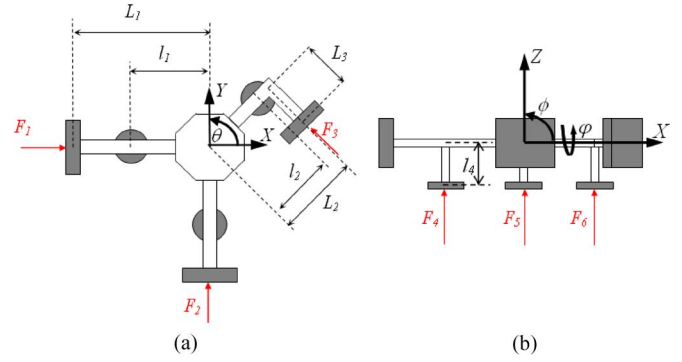Fig. 9.   Magnetic force along the y-axis in the impelling set.

Fig. 10.   Carrier structure and force relation. (a) Top view of the carrier. (b) Front view of the carrier.

those averaged data. The resulting fit is

$$F_{\mathrm{rec},y} = (a_6 y^6 + a_5 y^5 + a_4 y^4 + a_3 y^3 + a_2 y^2 + a_1 y + a_0) I_{\mathrm{rec}}$$
$$(8)$$

where $a_6 = -1.95 \times 10^9$, $a_5 = 4.39 \times 10^8$, $a_4 = -3.38 \times 10^7$, $a_3 = 1.16 \times 10^6$, $a_2 = -19338$, $a_1 = 214.8$, and $a_0 = -0.385$.

III. MODELING AND DYNAMIC FORMULATION

A. Assumptions

The following assumptions are made.
1) The carrier is made of an aluminum alloy, and we assume that it is a rigid body throughout its motion range.
2) The magnetic fields generated by any two actuating components can be viewed as decoupled.
3) Since the carrier's translation performance is the main concern in normal operation, the permissible angular displacement range and their rates are typically small. Thus, the attitude change around the z-axis is assumed not to be coupled with those around the other two axes. Additionally, we assume that the lateral dynamics will not influence those along the vertical axis.

B. Mathematical Modeling

To develop the general model for this system, the global coordinate is first defined. Its origin is located at the center of the carrier when it is at its nominal configuration. Based on Assumption 3, the terms of $\dot{\theta}\dot{\phi}$, $\dot{\phi}\dot{\varphi}$, and $\dot{\theta}\dot{\varphi}$ are exceedingly small. Thus, the torques which are the nonsymmetrical terms of the momentum, i.e., I_{XY}, I_{YZ}, I_{ZX}, I_{YX}, I_{ZY}, and I_{XZ}, multiplied by $\dot{\theta}\dot{\phi}$, $\dot{\phi}\dot{\varphi}$, and $\dot{\theta}\dot{\varphi}$, will be neglected. From the force relations in Fig. 10 and *Newton's Law*, the general dynamics of this system can be written as

$$\sum F_X = M\ddot{X} = F_1 - \frac{\sqrt{2}}{2} F_3$$

$$\sum F_Y = M\ddot{Y} = F_2 + \frac{\sqrt{2}}{2} F_3$$

$$\sum F_Z = M\ddot{Z} = F_4 + F_5 + F_6 - Mg$$

be justified to simplify $g_{\mathrm{cyl},z}(x,y,z)$ as a function with only a dependent variable z, and hence, we can write

$$F_{\mathrm{cyl},z} = g_{\mathrm{cyl},z}(z) I_{\mathrm{cyl}}. \qquad (5)$$

Based on this, we first average those three sets of data to produce the representative values at various z positions and then calculate the best fit fourth-order polynomial curve. The calculated result is

$$F_{\mathrm{cyl},z} = g_{\mathrm{cyl},z}(z) I_{\mathrm{cyl}} = (b_4 z^4 + b_3 z^3 + b_2 z^2 + b_1 z + b_0) I_{\mathrm{cyl}}$$
$$(6)$$

where $b_4 = -5.61 \times 10^6$, $b_3 = -4.89 \times 10^5$, $b_2 = -1.67 \times 10^4$, $b_1 = -219.34$, and $b_0 = 0.066$.

Fig. 8 shows the configuration of a pair of electromagnetic coils and PMs in the impelling set, where we set $y = 0$ at the coil center and let the total measuring range be $y \in [5\,\mathrm{mm}, 45\,\mathrm{mm}]$ from the center through the top surface to the outside of the rectangular coil. From this result, the measurements of $F_{\mathrm{rec},y}$ at different locations along the y-axis are all very close, with the largest deviation among the three data lines being less than 8% (referring to Fig. 9). By applying the same philosophy dealing with the maglev set to the present situation, we can also assume that the magnetic force on the rectangular PM is equal to the product of a nonlinear function of the PM's y position and the current flowing through the coil as

$$F_{\mathrm{rec},y} = g_{\mathrm{rec},y}(y) I_{\mathrm{rec}}. \qquad (7)$$

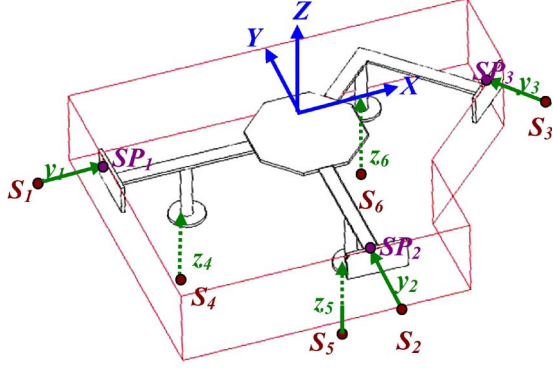The measurement results are shown in Fig. 9. Likewise, we calculate the best fit sixth-order polynomial curve based on

Fig. 11. Arrangement of optical sensors.

$$\sum T_X \cong I_{XX}\ddot{\varphi} + (I_{ZZ} - I_{YY})\dot{\phi}\dot{\theta}$$

$$\cong I_{XX}\ddot{\varphi} = -F_5 l_1 + \frac{\sqrt{2}}{2}F_6 l_2$$

$$\sum T_Y \cong I_{YY}\ddot{\phi} + (I_{XX} - I_{ZZ})\dot{\varphi}\dot{\theta}$$

$$\cong I_{YY}\ddot{\phi} = F_4 l_1 - \frac{\sqrt{2}}{2}F_6 l_2$$

$$\sum T_Z \cong I_{ZZ}\ddot{\theta} + (I_{YY} - I_{XX})\dot{\varphi}\dot{\phi} \cong I_{ZZ}\ddot{\theta} = F_3 L_3 \qquad (9)$$

where $M = 0.65$ kg is the carrier mass, and $L_3 = 0.075$ m, $l_1 = l_2 = 0.1$ m, $I_{XX} = 0.000101$ kg $\cdot$ m^2, $I_{YY} = 0.000101$ kg $\cdot$ m^2, and $I_{ZZ} = 0.00032$ kg $\cdot$ m^2.

This maglev system is controlled under 6-DOF feedback, so that there must exist at least six displacement detectors to measure six distinct displacements of the carrier in order to generate the carrier's position and attitude information, including three translations and three rotations. The proper arrangement of the six sensors (S_i, $i = 1$ to 6) is shown in Fig. 11. Initially, for every actuating component of the impelling sets, the PM is located at $y = p_{\text{rec},0} = 30$ mm in the local coordinate system. Similarly, each PM in each actuating component of the maglev sets is located at $z = p_{\text{cyl},0} = -20$ mm in the local coordinate system. Once the carrier undergoes a translation $[X, Y, Z]^T$ and a rotation $[\varphi, \phi, \theta]^T$, every PM's position will be recorded relative to its local coordinate. Therefore, three new relative y's in the three impelling sets and three new relative z's in the three maglev sets can be, respectively, expressed as

$$y_1' = p_{\text{rec},0} + X + L_1(1 - \cos\theta)$$

$$y_2' = p_{\text{rec},0} + Y + L_1(1 - \cos\theta)$$

$$y_3' = p_{\text{rec},0} + \frac{\sqrt{2}}{2}(-X + Y) + (L_2^2 + L_3^2)^{\frac{1}{2}}\sin\theta$$

$$z_4' = p_{\text{cyl},0} + Z + l_1 \sin\phi$$

$$z_5' = p_{\text{cyl},0} + Z - l_1 \sin\varphi$$

$$z_6' = p_{\text{cyl},0} + Z + \frac{\sqrt{2}}{2}l_2(\sin\varphi - \sin\phi) \qquad (10)$$

where $L_1 = 0.16$ m and $L_2 = 0.11$ m. By substituting (10) into (9), the forces with the subscripts 1–6 in (9) can be readily obtained. Then, the plant model can be rewritten in matrix form as

$$\overline{M}\ddot{\overline{X}} = B(\overline{Y}')\overline{U} - \overline{G} \qquad (11)$$

where $\overline{M} \equiv \text{diag}[M, M, M, I_{xx}, I_{yy}, I_{zz}]$, vectors $\equiv [X, Y, Z, \varphi, \phi, \theta]^T$, $\overline{Y} \equiv [y_1', y_2', y_3', z_4', z_5', z_6']^T$, $\overline{U} \equiv [I_1, I_2, I_3, I_4, I_5, I_6]^T$, $\overline{G} \equiv [0, 0, Mg, 0, 0, 0]^T$, and $B(\overline{Y}')$ is shown at the bottom of the page.

IV. CONTROLLER ANALYSIS

To realize the goals of precision positioning, a proper controller must be designed to control this maglev system. During the modeling process in the previous section, we have made several assumptions that will inevitably lead to some modeling errors. Therefore, the stabilizing controller developed here should be robust enough to tolerate these inherent uncertainties.

Up to now, there are several kinds of control methodologies available. One is the field of the adaptive control [18]–[22], which can tune the controller gains in real time or estimate the system's parameters to guarantee the stability of the closed-loop system. However, this kind of controller still has some pitfalls. For example, one is its poor transient response resulting from the real-time tuning process, and another is its poorer ability to deal with unmodeled dynamics and external disturbances. The second category is the field of robust controls, including, e.g., variable structure control [23], [25], H^∞ control [26], [29], and linear quadratic Gaussian (LQG) control [30], [31]. Among the existing robust control approaches, SMC has been recognized as an effective robust control approach for uncertain systems, and it has successfully been applied to a wide variety of practical engineering systems, such as robot manipulators, aircraft, underwater vehicles, spacecraft, flexible space structures, electrical motors, power systems, and automotive engines [29], [32]. The main features of SMC systems are the following: 1) fast response and good transient performance, and

$$B(\overline{Y}') \equiv \begin{bmatrix} g_{\text{rec}}(y_1') & 0 & -\frac{\sqrt{2}}{2}g_{\text{rec}}(y_3') & 0 & 0 & 0 \\ 0 & g_{\text{rec}}(y_2') & \frac{\sqrt{2}}{2}g_{\text{rec}}(y_3') & 0 & 0 & 0 \\ 0 & 0 & 0 & g_{\text{cyl}}(y_4') & g_{\text{cyl}}(y_5') & g_{\text{cyl}}(y_6') \\ 0 & 0 & 0 & 0 & -l_1 g_{\text{cyl}}(y_5') & \frac{\sqrt{2}}{2}l_2 g_{\text{cyl}}(y_6') \\ 0 & 0 & 0 & l_1 g_{\text{cyl}}(y_4') & 0 & -\frac{\sqrt{2}}{2}l_2 g_{\text{cyl}}(y_6') \\ 0 & 0 & L_2 g_{\text{rec}}(y_3') & 0 & 0 & 0 \end{bmatrix}$$

2) robustness against a large class of perturbations or model uncertainties. In fact, Maglev system without control is an open-loop unstable system, which makes the control issue here subtle and full of challenge, particularly being required to take care of several system uncertainties and disturbances. In order to possess the capability of real-time gain tuning as well as robustness, in this paper, we propose an ASMC [33]–[36], which will be described in the following in detail.

A. Linearization of System Model

Referring to the plant model shown by (11), for the purpose of the following controller design, it is linearized at the operating point $\overline{Y}'_0 = [0,0,0,0,0,0]^T$ by substituting $B_0 = B(\overline{Y}'_0)$ for the function B. Due to the carrier's gravity, we initially derive the bias currents flowing into the maglev sets to lift the carrier to some roughly leveling stage. Again, from (11), the bias currents are apparently

$$U_{\text{Bias}}$$
$$= B_0^{-1}\overline{G} \cdot$$

$$= \begin{bmatrix} 1.6674 & 0 & -1.179 & 0 & 0 & 0 \\ 0 & 1.6674 & 1.179 & 0 & 0 & 0 \\ 0 & 0 & 0 & 1.4769 & 1.4769 & 1.4769 \\ 0 & 0 & 0 & 0 & -0.1477 & 0.1149 \\ 0 & 0 & 0 & 0.1477 & 0 & -0.1149 \\ 0 & 0 & 0.20 & 0 & 0 & 0 \end{bmatrix}^{-1}$$

$$\times \begin{bmatrix} 0 \\ 0 \\ 6.1313 \\ 0 \\ 0 \\ 0 \end{bmatrix} = \begin{bmatrix} 0 \\ 0 \\ 0 \\ 1.2636 \\ 1.2636 \\ 1.6243 \end{bmatrix}. \tag{12}$$

Thus, the final input current of a coil is the sum of the output of one specific controller U_{Ctrl} and the associated bias U_{Bias}, i.e., $\overline{U} = U_{\text{Ctrl}} + U_{\text{Bias}}$; then, (11) can be obtained as a reference model

$$\overline{M}\ddot{\overline{X}} = B_0 U_{\text{Ctrl}}. \tag{13}$$

Nevertheless, because we made some assumptions to simplify the plant's model development in Section III, some inaccuracies of the resulting plant model will surely occur. To reflect this fact while considering the positioning task, we define an error state vector $E \equiv \overline{X} - \overline{X}_d$, where $\overline{X}_d$ is the desired position and $\overline{X}$ is the current position. As a result, (13) can be rewritten as

$$\overline{M}\ddot{E} = B_0 U_{\text{Ctrl}} - \overline{M}\ddot{\overline{X}}_d + W_1 \tag{14}$$

where W_1 denotes the system's uncertainty and is assumed bounded.

B. Adaptive Sliding-Mode Controller Design

In order to design a controller which possesses a better ability to gain high robustness and self-tuning property, two advanced control methods have been integrated. In this section, we will introduce the controller design and provide the stability analysis.

1) ASMC: From (14), we denote the term $\overline{M}^{-1}B_0$ as P and $\overline{M}^{-1}W_1$ as a constant uncertainty Q plus a varying uncertainty R. Therefore, (14) can be expressed as

$$\ddot{E} = PU_{AS} - \ddot{\overline{X}}_d + Q + R \tag{15}$$

where we assume that the varying uncertainty is bounded and $\|R\| \leq R_{\text{MAX}}$. Furthermore, we define the sliding surface variable S as

$$S = \dot{E} + \Lambda E \tag{16}$$

where Λ is a positive diagonal matrix. In this paper, we try to regulate the state error E to zero, and in the context of SMC, asymptotical convergence of the variable S to zero will apparently imply asymptotical convergence of E, and $\dot{E}$ as well, to zero. To validate this, we will need to investigate the dynamics of the sliding surface variable S as follows:

$$\dot{S} = \ddot{E} + \Lambda\dot{E} = (\Lambda\dot{E} - \ddot{\overline{X}}_d + Q + R) + PU_{AS}. \tag{17}$$

In addition to the SMC, an adaptive controller is applied for estimating the parameters of the system online while simultaneously controlling the system [16]. After we have the estimates of the system parameters, the control command in (17) can then adopt these estimates to form appropriate SMC with boundary layer as

$$U_{AS} = \hat{P}^{-1}\left(-KS - \Lambda\dot{E} - N \cdot sat(S/\varepsilon) + \ddot{\overline{X}}_d - \widehat{Q}\right) \tag{18}$$

where K and N are positive diagonal matrices with $\|N\| > R_{\text{MAX}}$, $\hat{P}$ and $\hat{Q}$ are the estimates of P and Q, respectively, and $sat(\cdot/\varepsilon)$ is the saturation function with boundary layer width ε. Notably, the use of saturation function instead of sign function $\text{sign}(\cdot)$ will naturally alleviate the so-called chattering problem.

Thus, substituting (18) into (17), we obtain

$$\dot{S} = (\Lambda\dot{E} - \ddot{\overline{X}}_d + Q + R)$$
$$+ P\left[\hat{P}^{-1}\left(-KS - \Lambda\dot{E} - N \cdot sat(S/\varepsilon) + \ddot{\overline{X}}_d - \hat{Q}\right)\right]$$
$$= -KS - N \cdot sat(S/\varepsilon) + R + \tilde{Q} + \tilde{P}U_{AS} \tag{19}$$

where the estimation errors are defined as $\tilde{P} = P - \hat{P}$ and $\tilde{Q} = Q - \hat{Q}$. By applying appropriate gains K, N, and Λ, we can ensure the convergence of S and, hence, the tracking error E to a neighborhood of zero, whose size depends on the boundary layer width ε, and meanwhile maintain the estimation errors within a bound.

2) Stability Analysis: We define a Lyapunov function candidate V, which is a positive definite function

$$V = \frac{1}{2}S^T S + \frac{1}{2}\text{tr}\left(\tilde{P}^T\Gamma_1^{-1}\tilde{P}\right) + \frac{1}{2}\text{tr}\left(\tilde{Q}^T\Gamma_2^{-1}\tilde{Q}\right) \tag{20}$$

where Γ_1^{-1} and Γ_2^{-1} are positive diagonal matrices. The time derivative of the Lyapunov candidate function V can be found to be

$$
\begin{aligned}
\dot{V} &= S^T \dot{S} + \mathrm{tr}\left(\tilde{P}^T \Gamma_1^{-1} \dot{\tilde{P}}\right) + \mathrm{tr}\left(\tilde{Q}^T \Gamma_2^{-1} \dot{\tilde{Q}}\right) \\
&= -S^T K S - S^T \left(N \cdot \mathrm{sat}(S/\varepsilon) - R\right) + S^T \tilde{P} U_{AS} \\
&\quad + S^T \tilde{Q} + \mathrm{tr}\left(\tilde{P}^T \Gamma_1^{-1} \dot{\tilde{P}}\right) + \mathrm{tr}\left(\tilde{Q}^T \Gamma_2^{-1} \dot{\tilde{Q}}\right) \\
&= -S^T K S - S^T \left(N \cdot \mathrm{sat}(S/\varepsilon) - R\right) \\
&\quad + \mathrm{tr}\left[\tilde{P}^T \left(\Gamma_1^{-1} \dot{\tilde{P}} + S U_{AS}^T\right)\right] +, \mathrm{tr}\left[\tilde{Q}^T \left(\Gamma_2^{-1} \dot{\tilde{Q}} + S\right)\right] . \quad (21)
\end{aligned}
$$

Using the σ-modification [15] of the adaptive control theory to establish boundedness of parameter estimates in the presence of modeling error terms, the adaptive laws are devised as

$$
\begin{aligned}
\dot{\hat{P}} &= -\dot{\tilde{P}} = \Gamma_1 S U_{AS}^T - \Gamma_1 \Sigma_1 \hat{P} \\
\dot{\hat{Q}} &= -\dot{\tilde{Q}} = \Gamma_2 S - \Gamma_2 \Sigma_2 \hat{Q}
\end{aligned} \quad (22)
$$

where $\Gamma_i \equiv \mathrm{diag}[\gamma_{i1} \; \gamma_{i2} \; \gamma_{i3} \; \gamma_{i4} \; \gamma_{i5} \; \gamma_{i6}]$ and $\Sigma_i \equiv \mathrm{diag}[\sigma_{i1} \; \sigma_{i2} \; \sigma_{i3} \; \sigma_{i4} \; \sigma_{i5} \; \sigma_{i6}] \; \forall i = 1, 2$ are all positive diagonal matrices. If these equations hold, (21) will become

$$
\begin{aligned}
\dot{V} &= -S^T K S - S^T \left(N \cdot \mathrm{sat}(S/\varepsilon) - R\right) \\
&\quad - \mathrm{tr}[\tilde{P}^T \Sigma_1 \hat{P}] - \mathrm{tr}[\tilde{Q}^T \Sigma_2 \hat{Q}] \\
&= -S^T K S - S^T \left(N \cdot \mathrm{sat}(S/\varepsilon) - R\right) \\
&\quad - \sum_{j=1}^{6} \left(\sigma_{1j} \tilde{p}_j^T \hat{p}_j + \sigma_{2j} \tilde{q}_j^T \hat{q}_j\right) \\
&\leq -S^T K S - S^T \left(N \cdot \mathrm{sat}(S/\varepsilon) - R\right) \\
&\quad - \sum_{j=1}^{6} \left\{\frac{\sigma_{1j}}{2}\left[\|\tilde{p}_j\|^2 - \|p_j\|^2\right] + \frac{\sigma_{2j}}{2}\left[|\tilde{q}_j|^2 - |q_j|^2\right]\right\} . \quad (23)
\end{aligned}
$$

After adding and subtracting the term αV for an adequate $\alpha > 0$, where $0 < \alpha < \min\{2k_j, \gamma_{1j}\sigma_{1j}, \gamma_{2j}\sigma_{2j}\} \; \forall j = 1-6$, we can obtain

$$
\begin{aligned}
\dot{V} &\leq -S^T \left(N \cdot \mathrm{sat}(S/\varepsilon) - R\right) - \alpha V \\
&\quad + \sum_{j=1}^{6} \left\{\frac{\sigma_{1j}}{2}\|p_j\|^2 + \frac{\sigma_{2j}}{2}|q_j|^2\right\} . \quad (24)
\end{aligned}
$$

Because the SMC scheme involving saturation function belongs to boundary layer control, the stability analysis should consider the effect of the boundary width ε. After considering two situations, namely, whether the sliding variable is inside the boundary layer or not, we can conclude the worst case bounded stability using the fact $-S^T(N \cdot \mathrm{sat}(S/\varepsilon) - R) \leq \|S\| \cdot R_{MAX}$, i.e., according to Lyapunov bounded stability theory, for

$$
V \geq V_0 = \frac{2}{\alpha} \sum_{j=1}^{6} \left\{\frac{1}{12\alpha} R_{MAX}^2 + \frac{\sigma_{1j}}{2}\|p_j\|^2 + \frac{\sigma_{2j}}{2}|q_j|^2\right\} \quad (25)
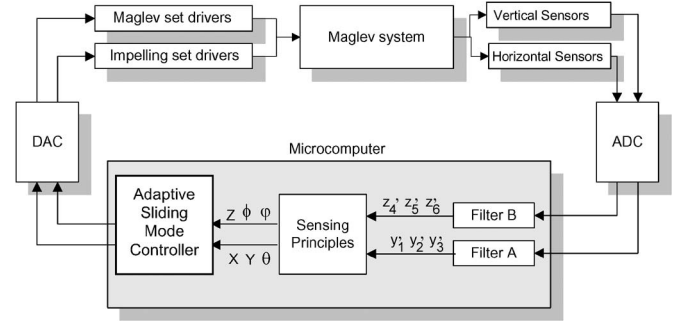$$

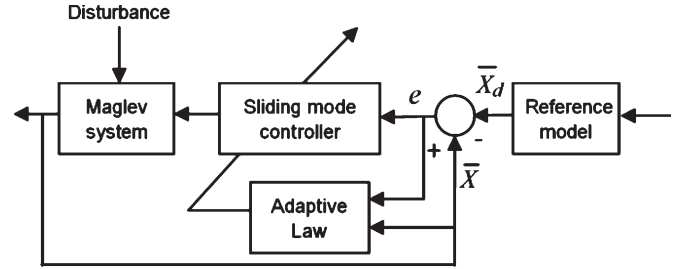Fig. 12. Control scheme block diagram of the closed-loop system.

Fig. 13. ASMC diagram.

we have $\dot{V} \leq 0$, which, in turn, implies that $V \in L_\infty$, where we also use the fact that $\|S\| \cdot R_{MAX} \leq 1/2\alpha \cdot \|S\|^2 + \alpha/2 \cdot R_{MAX}^2$. As a consequence, V and all signals in V, in particular, the estimate errors $\tilde{P}$ and $\tilde{Q}$, should be bounded on the order of $\max\{R_{MAX}, \sigma_{ij}^{1/2}\}$, whose fact when being substituted back to (19), namely,

$$
\dot{S} = -KS - (N \cdot \mathrm{sat}(S/\varepsilon) - R) + (\tilde{Q} + \tilde{P} U_{AS}) \quad (26)
$$

further implies that the tracking error $\|E(t)\|$ will converge to a residual set whose size is on the order of $\max\{\varepsilon, \sigma_{ij}^{1/2}/\lambda_{\min}(K), R_{MAX}/\lambda_{\min}(K)\}$. Of course, if the high gain N is chosen large enough, then the order will be as low as approximately ε only.

V. EXPERIMENTAL RESULTS

A. Hardware Setup

Fig. 3 shows the system setup. The material used for the PM, a critical factor to the success of the proposed system, was chosen to be NdFeB. To avoid electromagnetic interference effects and to meet the requirement of a long traveling range, optical sensors are adopted in this experiment. The model number of the optical sensor is Z4W-V25R, manufactured by the OMRON Corporation, Japan. Its sampling frequency is 10 kHz, and the active range is up to 8 mm with a resolution of 10 μm. Generally, such a sensor is fast enough and can cover the total specified range in this application. To avoid errors due to noise, we use a low-pass filter with a cutoff frequency of 10 kHz. The drivers are linear servo drivers for dc motors. The power is 250 W, 10 A at ±24 V. Based on the experimental results, a sampling time between 0.05 and 0.1 ms leads to better signal reconstruction through sampling. The analog-to-digital converter (ADC) is a 16-b high-resolution
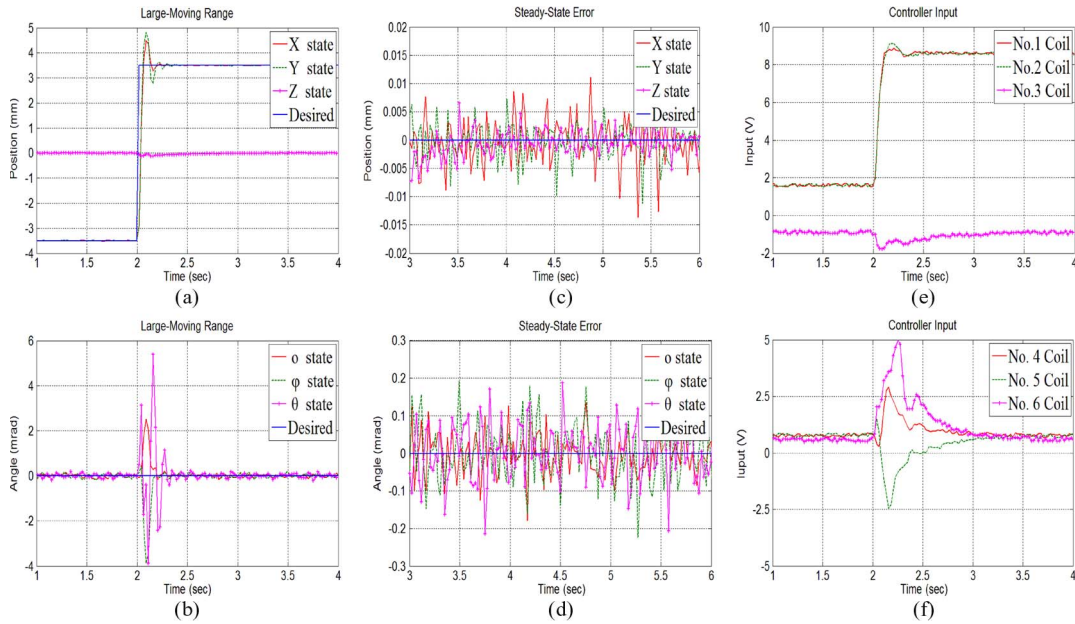
Fig. 14. Experimental results for regulating a large moving range (± 3.5 mm in both X- and Y-axes).
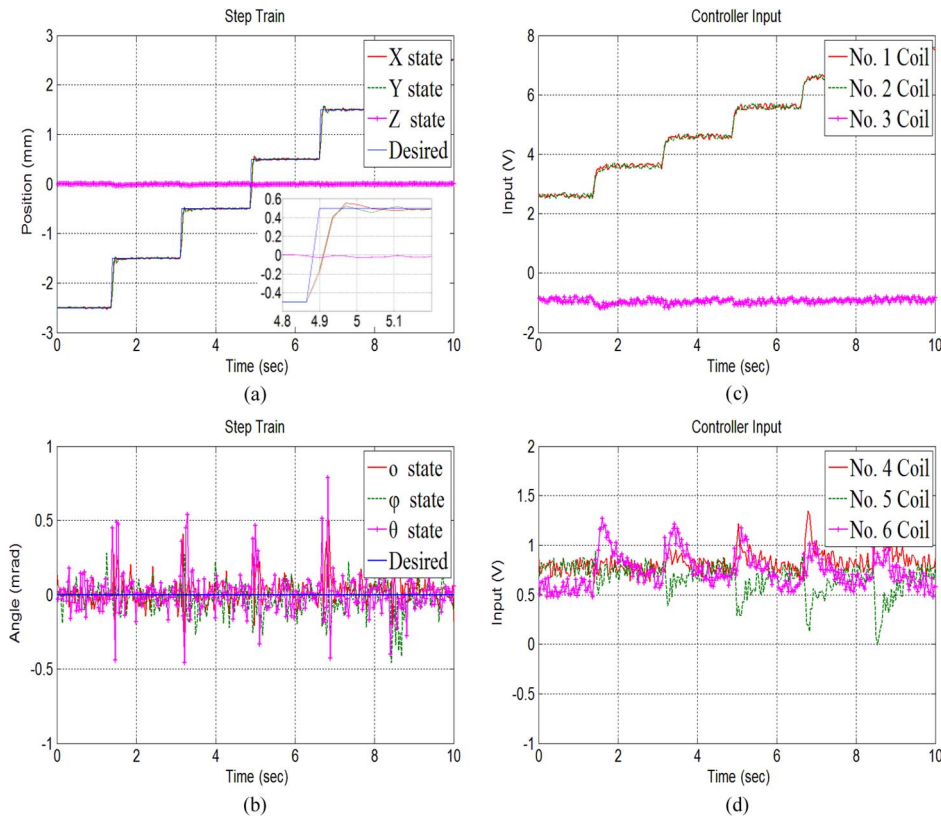

Fig. 15. Experimental result for repeating a 1-mm step-train response in X- and Y-axes.

data acquisition adapter and converts the analog sensor outputs to provide feedback to the digital controller. For the digital-to-analog converter (DAC) used to convert the control signals from digital to analog for compatibility with the drivers, there are altogether six converting channels with 12-b resolution each. Fig. 12 shows the control scheme block diagram of the closed-loop system. First, the vertical and horizontal sensors get the gap signals and import them to microcomputer by

ADC. Second, based on the sensing principle, filters A and B mean the low-pass filter whose bandwidth is set within 1 kHz. According to Fig. 11, the sensing principles are used to transfer six displacement detectors to six distinct displacements $(y_1', y_2', y_3', z_4', z_5', z_6')$ of the carrier into a translation (X, Y, Z) and a rotation (φ, ϕ, θ) by (10). Then, the digital controller produces the control signals to the maglev and impelling set drivers by DAC. The digital controller scheme is shown in
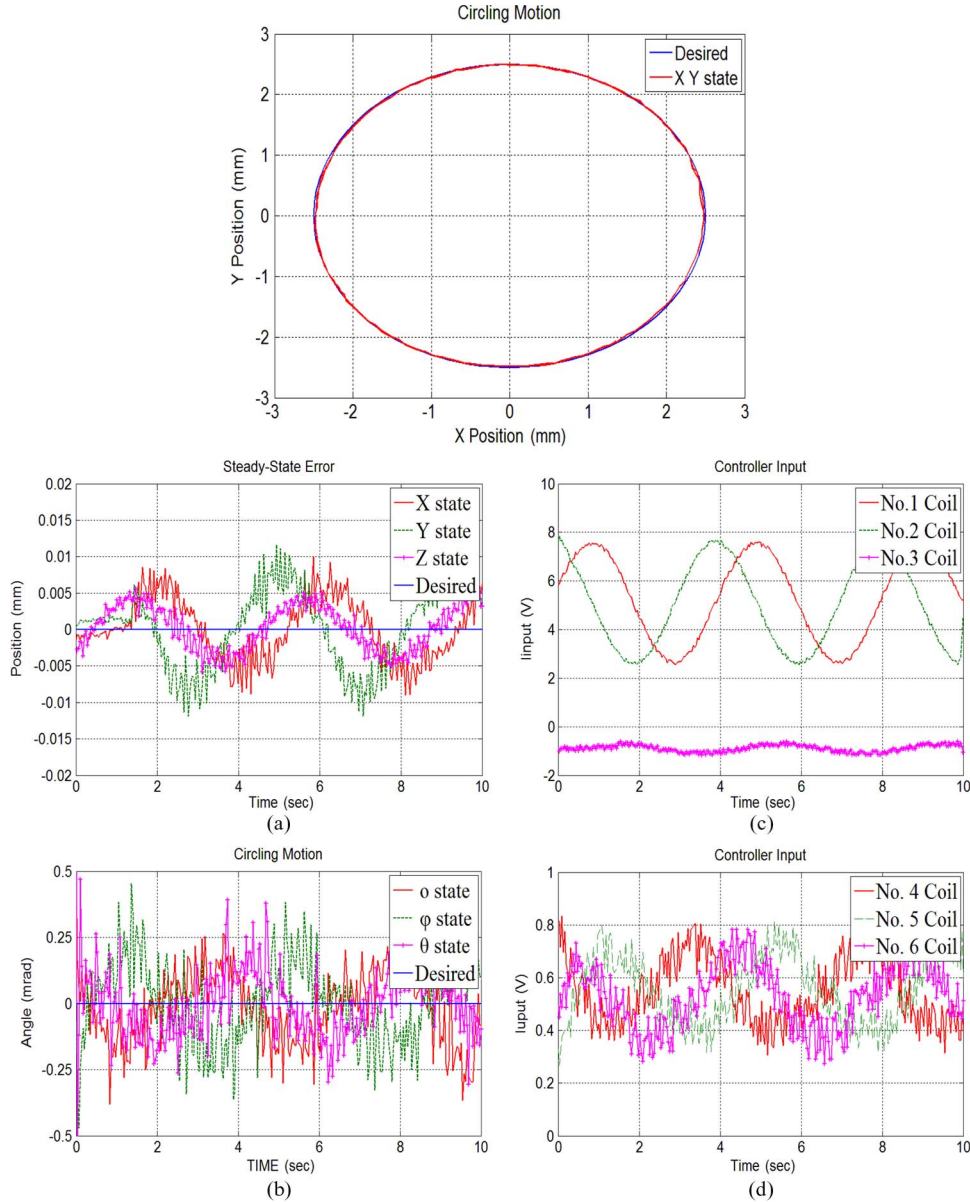
Fig. 16. Experimental result for tracking a sinusoidal motion at ± 2.5 mm with 0.25 Hz in X- and Y-axes.

Fig. 13. Based on the reference model and SMC structure for the Maglev system, the stable adaptive laws are designed to estimate the parameters in the presence of modeling error terms. Then, the parameters of the Maglev system are estimated prior to determining the control parameters which help to achieve the system objective. The labels in Figs. 14–17 are defined: (a) X state, (b) Y state, (c) Z state, (d) φ state, (e) ϕ state, and (f) θ state. The controller design parameters for the experiment are listed as follows:

$$\Lambda = \text{diag}[100, 100, 100, 100, 100, 100]^T$$
$$K = \text{diag}[10, 10, 10, 20, 20, 15]^T$$
$$N = \text{diag}[0.5, 0.5, 0.5, 1.5, 1.5, 1.5]^T$$
$$\Gamma_1 = \text{diag}[100, 100, 100, 100, 100, 100]^T$$
$$\Gamma_2 = \text{diag}[100, 100, 100, 100, 100, 100]^T.$$

B. Experiment Results

1) Large Moving Range: In order to test the available range of motion (millimeter level) of this system, we execute the XY plane positioning motion and let the other four states be regulated to zero, i.e., we set the initial 6-DOF configuration states to $X = -3.5$ mm, $Y = -3.5$ mm, and $Z = \varphi = \phi = \theta = 0$, and the control goal is to eventually converge these configuration states to the point at $X = 3.5$ mm, $Y = 3.5$ mm, and $Z = \varphi = \phi = \theta = 0$. The experimental data are shown in Fig. 14, where all configuration states except Z state can converge to the desired values within 0.5 s, whereas Z state takes 1 s to reach steady state and the steady-state errors are within the resolution level of the detecting sensors, i.e., 10 μm.

2) Step-Train Response: A continuing stepping response experiment with the proposed ASMC will be conducted with each step equal to 1 mm. The experimental result, as shown in Fig. 15, demonstrates the satisfactory performance in XY
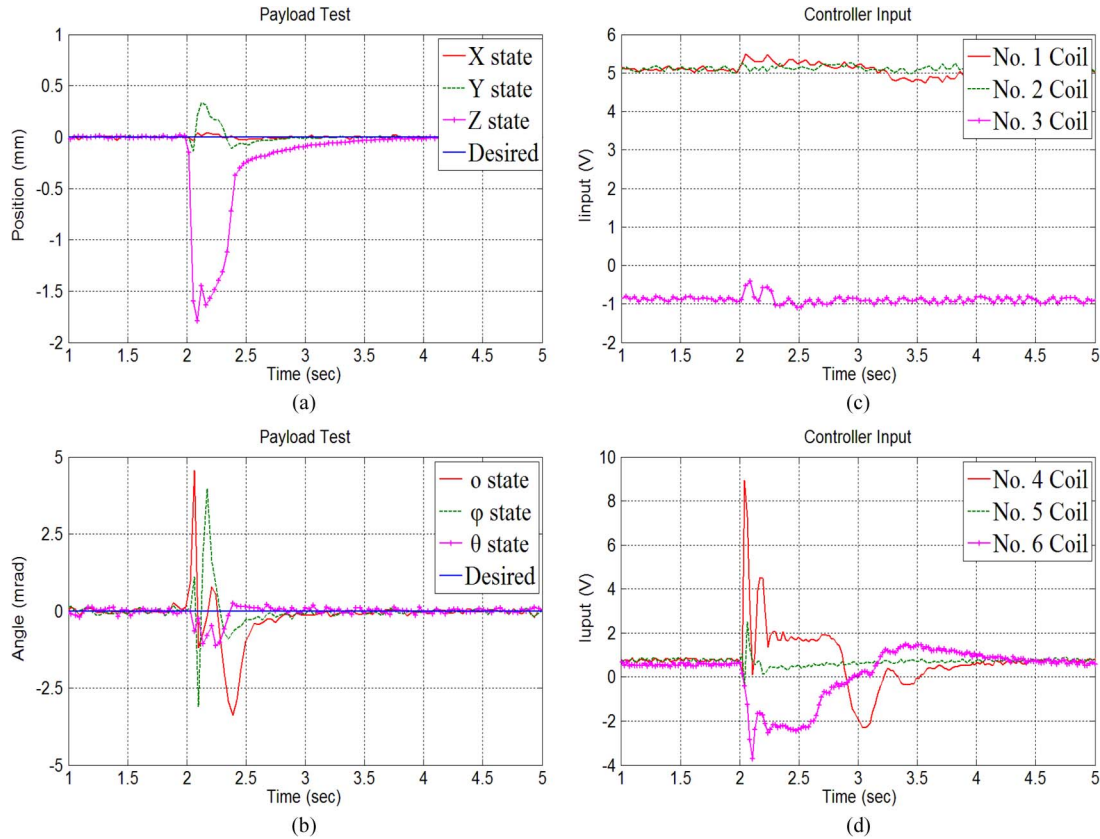
Fig. 17. Ability of the system to compensate for a disturbance (payload test 150 g).

plane motion where the transient time is within 0.15 s, which indicates that the settling time here is faster and all the steady-state errors are also within the resolution level of the detecting sensors. Although the motion dynamics for all the six states are coupled together, the strong robustness of the ASMC will, in fact, imply that XY step-train traversing will have little influence to the other four configuration states, namely, Z, φ, ϕ, and θ.

3) Circling Motion Response: In order to test the tracking capability, a way to show the tracking ability is to profile a desired circle. Fig. 16 shows the fine tracking ability on the XY plane where the trajectory traversed by the carrier almost perfectly overlaps the desired circle. The rms value for the tracking error is 13 μm which shows that the positioning performance attained the sensor's resolution limits, and the resolution is 10 μm which is the limit of the sensor resolution. Because of the higher robustness property of the ASMC, the coupling influences from the other four irrelevant configuration states, i.e., Z, φ, ϕ, and θ, become very small and are well within acceptable ranges. Continuing to increase the frequency of the target motion, we find that the highest frequency that this proposed ASMC can withstand is about 3.5 Hz.

4) Payload Test (150 g): In order to further validate the robustness of this system with the controller, a 150 g weighted mass (about one-fourth the weight of the carrier) is suddenly released from a 1-mm height right above the carrier. Fig. 17 shows that a payload which is suddenly set free vertically will have only a slight influence on every state and that it takes only around 1 s to return to each state's initial position. Again, this result shows the extreme robustness of the hereby developed ASMC.

VI. CONCLUSION

In this paper, we have designed and implemented a macro–micro 6-DOF maglev positioning system, which, in nature, serves as a multi-input multioutput system. To precisely regulate the 6 DOF and to track a particular desired motion, an ASMC is properly designed. To demonstrate the effectiveness of the system design and satisfactory performance of the precision positioning, extensive experiments have been conducted, and the results showed that the positioning performance reaches the limit of the sensor's resolution, namely, 10 μm, and the digital signal acquisition device and, moreover, the system's response suits practical applications. To sum up, the main contribution of this paper is the design of a new structure for a high-precision and long-range motion positioner, which successfully demonstrates feasibility and effectiveness of such a new system through extensive experimental results.

REFERENCES

[1] H. M. Hasanien, "Particle swarm design optimization of transverse flux linear motor for weight reduction and improvement of thrust force," *IEEE Trans. Ind. Electron.*, vol. 58, no. 9, pp. 4048–4056, Sep. 2011.

[2] I.-Y. Wang, "A magnetic levitation silicon wafer transport system," Ph.D. dissertation, Univ. Texas Austin, Austin, TX, 1993.

[3] M.-Y. Chen, M.-J. Wang, and L.-C. Fu, "A novel dual-axis repulsive maglev guiding system with permanent magnet: Modeling and controller design," *IEEE/ASME Trans. Mechatronics*, vol. 8, no. 1, pp. 77–86, Mar. 2003.

[4] W.-J. Kim and D. L. Trumper, "Active multivariable optimal control of a planar magnetic levitator," in *Proc. IEEE Int. Conf. Control Appl.*, Harford, CT, 1997, pp. 97–102.

[5] W.-J. Kim and H. Maheshwari, "High-precision control of a maglev linear actuator with nanopositioning capability," in *Proc. Amer. Control Conf.*, 2002, vol. 5, pp. 4279–4284.

[6] H. Shakir and W.-J. Kim, "Nanoscale path planning and motion control with maglev positioners," *IEEE/ASME Trans. Mechatronics*, vol. 11, no. 5, pp. 625–633, Oct. 2006.

[7] Y.-C. Lai and J.-Y. Yen, "A research in the application of permanent magnets and solenoids to the planar Maglev system design," in *Proc. IEEE Int. Conf. Magn.*, 2003, p. HB-10.

[8] K. S. Jung and Y. S. Baek, "Contact-free moving-magnet type of micropositioner with optimized specification," *IEEE Trans. Magn.*, vol. 38, no. 3, pp. 1539–1548, May 2002.

[9] Z. Zhang and C.-H. Menq, "Six-axis magnetic levitation and motion control," *IEEE Trans. Robot.*, vol. 23, no. 2, pp. 196–205, Apr. 2007.

[10] M.-Y. Chen, H.-W. Tzeng, and S.-K. Hung, "A new mechanism design of electro-magnetic actuator for a micro-positioner," *ISA Trans.*, vol. 46, no. 1, pp. 41–48, Feb. 2007.

[11] P. K. Sinha, *Electromagnetic Suspension: Dynamics and Control*. London, U.K.: Peregrinus, 1987.

[12] B. Cranganu-Cretu, A. Kertesz, and J. Smajic, "Coupled electromagnetic–thermal effects of stray flux: Software solution for industrial application," *IEEE Trans. Ind. Electron.*, vol. 57, no. 1, pp. 14–21, Jan. 2010.

[13] I. Martins, J. Esteves, G. D. Marques, and F. Pina da Silva, "Permanent-magnets linear actuators applicability in automobile active suspensions," *IEEE Trans. Veh. Technol.*, vol. 55, no. 1, pp. 86–94, Jan. 2006.

[14] S.-M. Yang, "Electromagnetic actuator implementation and control for resonance vibration reduction in miniature magnetically levitated rotating machines," *IEEE Trans. Ind. Electron.*, vol. 58, no. 2, pp. 611–617, Feb. 2011.

[15] D. K. Bae, H. J. Cho, and J. M. Lee, "Characteristic analysis of HTS levitation force with various conditions of ground conductors," *IEEE Trans. Appl. Supercond.*, vol. 18, no. 2, pp. 803–807, Jun. 2008.

[16] R. Zhaohui and L. S. Stephens, "Closed-loop performance of a six degree-of-freedom precision magnetic actuator," *IEEE/ASME Trans. Mechatronics*, vol. 10, no. 6, pp. 666–674, Dec. 2005.

[17] R. Prieto, J. Ã. Oliver, J. A. Cobos, and M. Christini, "Magnetic component model for planar structures based on transmission lines," *IEEE Trans. Ind. Electron.*, vol. 57, no. 5, pp. 1663–1669, May 2010.

[18] K. Khorasani, "A robust adaptive control design for a class of dynamical systems using corrected models," *IEEE Trans. Autom. Control*, vol. 39, no. 8, pp. 1726–1732, Aug. 1994.

[19] Y. Sun, M. Su, X. Li, H. Wang, and W. Gui, "Indirect four-leg matrix converter based on robust adaptive back-stepping control," *IEEE Trans. Ind. Electron.*, vol. 58, no. 9, pp. 4288–4298, Sep. 2011.

[20] C. Hu, B. Yao, and Q. Wang, "Adaptive robust precision motion control of systems with unknown input dead-zones: A case study with comparative experiments," *IEEE Trans. Ind. Electron.*, vol. 58, no. 6, pp. 2454–2464, Jun. 2011.

[21] L. Zuo, J.-J. E. Slotine, and S. A. Nayfeh, "Model reaching adaptive control for vibration isolation," *IEEE Trans. Control Syst. Technol.*, vol. 13, no. 4, pp. 611–617, Jul. 2005.

[22] L. Xu and B. Yao, "Adaptive robust precision motion control of linear motors with negligible electrical dynamics: Theory and experiments," *IEEE/ASME Trans. Mechatronics*, vol. 6, no. 4, pp. 444–452, Dec. 2001.

[23] S. Sayeef, G. Foo, and M. F. Rahman, "Rotor position and speed estimation of a variable structure direct-torque-controlled IPM synchronous motor drive at very low speeds including standstill," *IEEE Trans. Ind. Electron.*, vol. 57, no. 11, pp. 3715–3723, Nov. 2010.

[24] C. Mademlis and I. Kioskeridis, "Gain-scheduling regulator for high-performance position control of switched reluctance motor drives," *IEEE Trans. Ind. Electron.*, vol. 57, no. 9, pp. 2922–2931, Sep. 2010.

[25] S. Suzuki, Y. Pan, and K. Furuta, "VS-control with time-varying sliding sector—Design and application to pendulum," *Asian J. Control*, vol. 6, no. 3, pp. 307–316, Sep. 2004.

[26] K. Watanabe, S. Hara, Y. Kanemitsu, T. Haga, K. Yano, T. Mizuno, and R. Katamura, "Combination of H^∞ and PI control for an electromagnetically levitated vibration isolation system," in *Proc. IEEE Conf. Decision Control*, 1996, vol. 2, pp. 1223–1228.

[27] R. Wang, G.-P. Liu, W. Wang, D. Rees, and Y.-B. Zhao, "H^∞ control for networked predictive control systems based on the switched Lyapunov function method," *IEEE Trans. Ind. Electron.*, vol. 57, no. 10, pp. 3565–3571, Oct. 2010.

[28] B. Hencey and A. G. Alleyne, "A robust controller interpolation design technique," *IEEE Trans. Control Syst. Technol.*, vol. 18, no. 1, pp. 1–10, Jan. 2010.

[29] S. Islam and X. P. Liu, "Robust sliding mode control for robot manipulators," *IEEE Trans. Ind. Electron.*, vol. 58, no. 6, pp. 2444–2453, Jun. 2011.

[30] C. S. Chang and T. S. Liu, "LQG controller for active vibration absorber in optical disk drive," *IEEE Trans. Magn.*, vol. 43, pt. 2, no. 2, pp. 799–801, Feb. 2007.

[31] F. D. Bruyne, B. D. O. Anderson, and M. Gevers, "On plant and LQG controller continuity questions," *Automatica*, vol. 34, no. 5, pp. 631–635, May 1998.

[32] J. Zhang and Y. Xia, "Design of static output feedback sliding mode control for uncertain linear systems," *IEEE Trans. Ind. Electron.*, vol. 57, no. 6, pp. 2161–2170, Jun. 2010.

[33] T. Orlowska-Kowalska, M. Dybkowski, and K. Szabat, "Adaptive sliding-mode neuro-fuzzy control of the two-mass induction motor drive without mechanical sensors," *IEEE Trans. Ind. Electron.*, vol. 57, no. 2, pp. 553–564, Feb. 2010.

[34] Y. Chang, "Adaptive sliding mode control of multi-input nonlinear systems with perturbations to achieve asymptotical stability," *IEEE Trans. Autom. Control*, vol. 54, no. 12, pp. 2863–2869, Dec. 2009.

[35] S. N. Huang, K. K. Tan, and T. H. Lee, "Adaptive sliding-mode control of piezoelectric actuator," *IEEE Trans. Ind. Electron.*, vol. 56, no. 9, pp. 3514–3522, Sep. 2009.

[36] Y. Li and Q. Xu, "Adaptive sliding mode control with perturbation estimation and PID sliding surface for motion tracking of a piezo-driven micromanipulator," *IEEE Trans. Control Syst. Technol.*, vol. 18, no. 4, pp. 798–810, Jul. 2010.

Mei-Yung Chen received the B.S. degree from Tamkang University, New Taipei, Taiwan, in 1992, the M.S. degree from Chungyuan Christian University, Chung Li, Taiwan, in 1994, and the Ph.D. degree from National Taiwan University, Taipei, Taiwan, in 2003.

He is currently an Associate Professor with the Department of Mechatronic Technology, National Taiwan Normal University, Taipei. His areas of research interest include magnetic levitation, positioning and tracking, mechatronics, and control theory and applications.

Tzuo-Bo Lin was born in Taipei, Taiwan, in 1979. He received the B.S. degree in mechanical engineering and the M.S. degree in electrical engineering from National Taiwan University, Taipei, Taiwan, in 2001 and 2003, respectively.

Since 2003, he has been with Realtek Semiconductor Corporation, Hsinchu, Taiwan, where he is currently a Planning Manager. His current research interests include audio system and video deinterlace technique in multimedia system.

Shao-Kang Hung (M'03) received the B.S., M.S., and Ph.D. degrees from National Taiwan University, Taipei, Taiwan, in 1998, 2000, and 2007, respectively.

Since 2008, he has been a Faculty Member with the Department of Mechanical Engineering, National Chiao Tung University, Hsinchu, Taiwan, where he is currently an Assistant Professor. His research interests include optomechatronic systems, nanometer-scale instrumentation, precision motion control, and robotics.

Li-Chen Fu (F'04) received the B.S. degree from National Taiwan University, Taipei, Taiwan, in 1981 and the M.S. and Ph.D. degrees from the University of California, Berkeley, in 1985 and 1987, respectively.

Since 1987, he has been with National Taiwan University, where he has been a Faculty Member and is currently a Full Professor with the Department of Electrical Engineering and Department of Computer Science and Information Engineering. His research interests include precision motion control, robotics, smart home, visual detection and tracking, intelligent vehicle, evolutionary optimization, virtual reality, and nonlinear control. He currently serves as the Editor-in-Chief of *Asian Journal of Control*.

Dr. Fu was invited to serve as a Distinguished Lecturer of IEEE Robotics and Automation Society during 2004-2005 and in 2007. He was a recipient of the Lifetime Distinguished Professorship from National Taiwan University in 2007. He was also a recipient of numerous academic recognitions, such as Distinguished Research Awards from National Science Council, Taiwan, and the Irving T. Ho Chair Professorship.